

M⁴Fuse: Lightweight State-Space MoE with a Cross-Scale Gating Bridge for Brain Tumor Segmentation

Meihua Zhou^{1*} Xinyu Tong^{1*†} Li Yang^{2†}

¹University of Chinese Academy of Sciences ²Wannan Medical University

{zhoumeihua25, tongxinyu25}@mailsucas.ac.cn, yangli@wnmc.edu.cn

Abstract

Encoder-decoder imbalance and the reliance on large input volumes make many 3D brain tumor segmentation models both compute-heavy and brittle. We present M⁴Fuse, a lightweight network that prioritizes discriminative brain tumor cues over exhaustive appearance reconstruction. Our method balances encoder and decoder capacity and replaces depth expansion with a synergistic design: it propagates long-range context with linear complexity via a grouped state space mixer, denoises and aligns skip features using a cross-scale dual-stage gating bridge, and absorbs cross-site acquisition shifts with a sample-level mixture-of-experts. On the BraTS2019 and BraTS2021 benchmarks, M⁴Fuse outperforms other lightweight excellent methods in both parameter count and performance. Even at a challenging input resolution of $64 \times 128 \times 128$ (half that of existing excellent models), M⁴Fuse reduces parameters by 62.63% and improves average performance by 0.09%. Ablations of key components validate the method’s exceptional parameter-to-accuracy efficiency and robustness across diverse data centers.

1. Introduction

Multimodal three dimensional brain tumor segmentation in clinical settings faces three coupled demands [2, 23, 46]. The model must capture long range three dimensional context in a memory efficient way, it must remain robust under cross site and cross protocol variation, and it must be lightweight for deployment [20]. The enhancing tumor is contrast dependent and small in volume and thin at the boundary, therefore it is highly sensitive to smoothing from normalization, upsampling, and cross scale fusion, and it is critical for clinical reading [16, 44].

In end to end encoder decoder architectures the balance of parameters strongly affects performance and efficiency

(a high leverage phenomenon in which small changes in the encoder to decoder ratio can cause large shifts in information flow and optimization). An over heavy encoder with an under powered decoder can produce features that the decoder cannot reconstruct faithfully, which creates a representational bottleneck and wastes encoder capacity [17, 22]. The opposite starves early evidence and shifts capacity to later stages, which weakens local cues and can destabilize training. Adding global modules in early encoder layers can increase complexity without commensurate gains [24, 43]. Popular plug in components such as efficient decoders and efficient encoders are useful, but blindly reducing complexity on a single side is not a universal solution, because it can harm accuracy, generalization, and multi task or multi expert processing.

We revisit input sizing without assuming a fixed cube. While many recent three dimensional pipelines standardize to $128 \times 128 \times 128$ to accommodate heavy encoders, we also report results at $128 \times 128 \times 128$. We deliberately relax this convention and explore $64 \times 128 \times 128$, which reduces the voxel budget and memory footprint and under our design preserves or improves accuracy. Capacity is placed where it pays off, with a grouped state space mixer supplying long range modeling in linear time while keeping local cues, a cross scale dual stage gating bridge that denoises in space and then realigns channels so the decoder receives clean and consistent skips, and sample level domain experts confined to high semantic low resolution layers, namely at the fourth and fifth encoder stages and at the bottleneck, to absorb center and protocol shifts with minimal overhead. The total number of parameters grows linearly with the number of experts, which keeps scaling controllable.

With purified and aligned skip connections the marginal utility of widening the high semantic or decoder path is low [27, 38]. On the BraTS series our base model with 1.11 million parameters achieves the best or tied Dice and HD95 while wider variants do not deliver significant average gains and can degrade the enhancing tumor. This observation forms a decoder marginal utility principle for medical three dimensional segmentation. Capacity controlled selectivity

*Equal contribution [github: {mh-zhou, tonxycs} / M4Fuse](https://github.com/mh-zhou,tonxycs/M4Fuse)

†Corresponding author

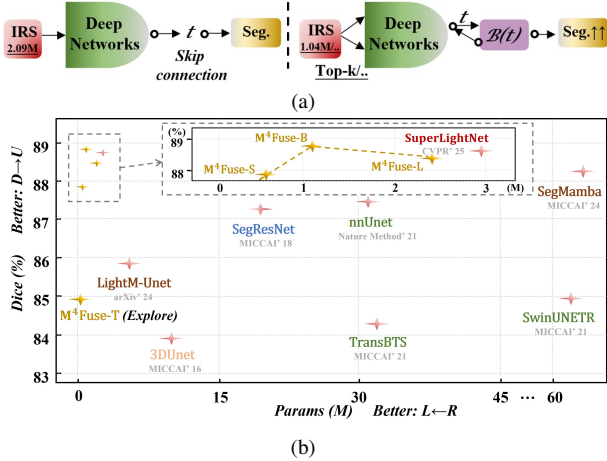


Figure 1. (a) On the left is a standard segmentation architecture, while the right integrates an expert mechanism with a unique attention bridge. The input resolution sequential length (IRS) of 1.04M/2.09M is used to validate the model’s generalisation capability. The number of experts is then allocated based on the structures, modalities and types of input data. This is followed by the feature extraction and segmentation processes. The number of allocated experts influences the parameter count and exhibits a positive correlation with it. (b) Visual comparison of lightweight medical segmentation methods versus other excellent methods on the BraTS 2021 dataset, based on Dice metrics, using input resolution sequence lengths as short as 1.04M.

is more important than widening the decoder.

We propose M⁴Fuse, a lightweight U shaped framework that embodies these choices. PetaloMixer supplies linear time long range context in mid and late pathways and before each upsampling step. CSBridge applies spatial denoising and cross scale channel realignment so that skip features are consistent and informative. The sample level expert unit adapts only high semantic layers, which avoids dragging early features toward site specific statistics and preserves low complexity at small input resolution.

Our contributions are as follows:

- We introduce a lightweight and deployment friendly three dimensional framework that combines a grouped state space mixer with a cross scale dual stage gating bridge and achieves strong accuracy with 1.11 million parameters.
- Sample-level domain experts, confined to high-semantic, low-resolution layers, are introduced, ensuring robustness to site and protocol variation while keeping parameters linearly controllable with expert count.
- A decoder marginal utility principle for medical three dimensional segmentation is identified, indicating that widening the high semantic or decoder path yields negligible average gains and can harm contrast dependent micro structures such as the enhancing tumor.
- We present core-parameter ablations and an accuracy-

parameter Pareto analysis, showing the base configuration lies on the Pareto frontier in the small-input regime.

2. Related Work

2.1. Multimodal Fusion and Adaptive Routing

Early multimodal MRI segmentation mainly explored early, middle, and late fusion. Early fusion concatenates modalities at the input and learns a shared encoder [21]; middle fusion uses separate encoders and merges features at intermediate or bottleneck layers, preserving modality-specific representations but typically limiting interaction to a single stage and increasing memory and computation [25, 26]; and late fusion combines deep features or predictions near the output, offering flexibility but weaker access to fine-grained cross-modal cues [1]. To strengthen interaction, prior work introduced cross-modal attention and gating for spatially adaptive weighting and feature exchange [30, 33, 40], dense cross-links for multi-depth feature reuse [30], and cross-modality alignment for unregistered inputs [13]. However, these designs often incur high activation and training costs [40], and most model interaction at only one or two scales without explicit cross-scale consistency [21, 33]. Related studies in industrial and vision tasks likewise highlight the value of multiscale guidance, bidirectional cues [28], and application-driven attention [8]. MoE routing further decouples modality-specific capacity by selecting experts per sample or region [9, 14, 34], reducing cross-modal interference and improving robustness to scanner and site variation [7, 10]; however, expert collapse, load imbalance, and additional latency and memory overhead remain key challenges [3, 5, 37, 39, 45]. Related task-adaptive routing has also shown promise in medical image restoration [35], but its integration with multi-scale fusion and decoder skip connections remains underexplored.

2.2. Lightweight Multimodal Brain Segmentation

Transformer token mixers such as UNETR and Swin UNETR improve volumetric segmentation by modeling long-range context, but remain expensive in 3D due to the cost of attention over many tokens and the need for deep stacks [11, 24, 29]. Efficient attention reduces complexity through factorization or linearization, yet stable, budget-matched high-resolution performance is still difficult [15, 32, 41]. State space models provide linear-complexity sequence mixing and have been adopted in 3D encoders and U-shaped backbones [31], but key issues remain in preserving 3D locality, aggregating multiple scan directions, and integrating sequence mixing into decoder stages dominated by upsampling and multi-scale fusion. In parallel, lightweight 3D CNN designs and compression techniques reduce parameters and FLOPs through efficient convolutions, pruning, and distillation [6, 18, 36, 42], but

may weaken channel interaction, global reasoning, and robustness to domain shift, especially for small lesions and boundaries [4]. Accordingly, BraTS evaluation still centers on Dice and HD95 [12], while efficiency metrics such as parameters, FLOPs, and latency are becoming increasingly important in lightweight segmentation.

3. Method

3.1. Overview

Volumetric brain tumor segmentation with multimodal MRI requires three properties at once. The network must propagate long-range context across depth, height, and width in a memory-efficient way. The decoder must receive skip connections that are denoised and consistent across scales to avoid redundant or conflicting activations. The representation must adapt across acquisition differences while keeping the parameter budget very small (see Figure 2). We introduce M⁴Fuse, which realizes these properties with a lightweight U-shaped backbone. A grouped state-space mixer (POM) provides global context in the mid and late pathway. A cross-scale dual-stage gating bridge (CSB) purifies and aligns encoder features before decoding. A shared-plus-expert unit (PEU) adapts high-level features across centers. The input is $x \in \mathbb{R}^{B \times C \times D \times H \times W}$ where B is the mini-batch size, C is the number of input channels corresponding to modalities, D, H, W are spatial sizes, and $C = 4$ on BraTS. Encoder outputs at five scales are $t_s \in \mathbb{R}^{B \times C_s \times D_s \times H_s \times W_s}$ for $s \in \{1, 2, 3, 4, 5\}$ with resolution decreasing as s increases. The deepest representation is the bottleneck b . The bridge transforms $\{t_s\}_{s=1}^5$ into $\{\tilde{t}_s\}_{s=1}^5$ which are reused in the decoder. The decoder proceeds from b through three stages d_1, d_2, d_3 . We denote decoder activations by $d_k \in \mathbb{R}^{B \times C_{d_k} \times D_{d_k} \times H_{d_k} \times W_{d_k}}$ for $k \in \{1, 2, 3\}$. At each stage it first applies the mixer, then upsamples, then fuses with the bridged feature at the matched resolution, so d_1 fuses with \tilde{t}_5 , d_2 fuses with \tilde{t}_4 , d_3 fuses with \tilde{t}_3 . The expert unit, applied at t_4, t_5 , and b and its runtime scales linearly with the number of voxels.

3.2. Grouped State Space Mixer

A three-dimensional tensor is reshaped into a sequence that preserves voxel order in a fixed raster-scan order. Layer normalization is $\text{LN}(\cdot)$ and LN acts on the channel axis. The reshape stacks spatial locations into length L . The transpose $(\cdot)^\top$ swaps the last two axes so that the sequence length becomes the second axis. Concatenation along channels is $[\cdot \parallel \cdot]$. We write

$$\begin{cases} X = \text{LN}(\text{reshape}(x; B, C, L))^\top \in \mathbb{R}^{B \times L \times C}, \\ L = D H W, \end{cases} \quad (1)$$

where L is the number of voxels and C is the channel width. The channel axis is partitioned into g equal groups and we

use $g = 4$. Let

$$X = [X^{(1)} \parallel \dots \parallel X^{(g)}], \quad X^{(j)} \in \mathbb{R}^{B \times L \times C/g}.$$

Each group is scanned by a discrete state-space model along the sequence index $k \in \{1, \dots, L\}$. The hidden state is $h_k^{(j)} \in \mathbb{R}^{B \times d^{(j)}}$, where $d^{(j)}$ is the state dimension for group j . The system matrices are $A^{(j)} \in \mathbb{R}^{d^{(j)} \times d^{(j)}}$, $B^{(j)} \in \mathbb{R}^{d^{(j)} \times (C/g)}$, $C^{(j)} \in \mathbb{R}^{(C/g) \times d^{(j)}}$. With step size $\Delta > 0$ the discrete recursion is

$$\begin{cases} h_{k+1}^{(j)} = \bar{A}^{(j)} h_k^{(j)} + \bar{B}^{(j)} X_k^{(j)}, \\ Y_k^{(j)} = C^{(j)} h_k^{(j)}, \end{cases} \quad k = 1, \dots, L, \quad (2)$$

where $Y_k^{(j)} \in \mathbb{R}^{B \times (C/g)}$ is the group output at position k . The matrices $\bar{A}^{(j)} \in \mathbb{R}^{d^{(j)} \times d^{(j)}}$ and $\bar{B}^{(j)} \in \mathbb{R}^{d^{(j)} \times (C/g)}$ are the discretized transition and input maps obtained from a continuous linear system by a matrix exponential. The matrix exponential is $\exp(\cdot)$. We write

$$\begin{cases} \bar{A}^{(j)} = \exp(A^{(j)} \Delta), \\ \bar{B}^{(j)} = \int_0^\Delta \exp(A^{(j)} \tau) B^{(j)} d\tau. \end{cases} \quad (3)$$

Stacking over k yields $\text{SSM}(X^{(j)}) \in \mathbb{R}^{B \times L \times (C/g)}$ whose k th slice equals $Y_k^{(j)}$. A learnable nonnegative residual scale $s \in \mathbb{R}_{\geq 0}$ stabilizes narrow widths

$$Z^{(j)} = \text{SSM}(X^{(j)}) + s X^{(j)}. \quad (4)$$

Group outputs are concatenated, normalized, and linearly projected with $W \in \mathbb{R}^{C \times C_{\text{out}}}$ where C_{out} is the output width

$$\begin{cases} Z = \text{LN}([Z^{(1)} \parallel \dots \parallel Z^{(g)}]) \in \mathbb{R}^{B \times L \times C}, \\ U = Z W \in \mathbb{R}^{B \times L \times C_{\text{out}}}. \end{cases} \quad (5)$$

Finally U is reshaped to $\mathbb{R}^{B \times C_{\text{out}} \times D \times H \times W}$. The scan in each group has cost $\mathcal{O}(L C/g)$ so the mixer is linear in L . Attention has cost $\mathcal{O}(L^2 C)$. The mixer is inserted at t_4, t_5 , and b and at each decoder stage before upsampling to keep global information along the reconstruction path. Let $\rho(\cdot)$ be the spectral radius and let $\|\cdot\|$ be any submultiplicative operator norm. Let $\|X^{(j)}\| := \sup_k \|X_k^{(j)}\|$. If $\rho(\bar{A}^{(j)}) \leq 1$ then, using submultiplicativity and the uniform bound on $\|X_k^{(j)}\|$, the sequence defined by (2) and (4) satisfies

$$\begin{cases} \|Z^{(j)}\| \leq \kappa \|X^{(j)}\| + s \|X^{(j)}\|, \\ \kappa = \sup_k \|C^{(j)}\| \sum_{t=0}^k \|\bar{A}^{(j)}\|^t \|\bar{B}^{(j)}\|. \end{cases} \quad (6)$$

When $\|\bar{A}^{(j)}\| < 1$ the sum is dominated by a geometric bound. The direct term with scale s prevents vanishing or exploding responses in long scans and the normalizations in (1) and (5) bound feature-scale drift.

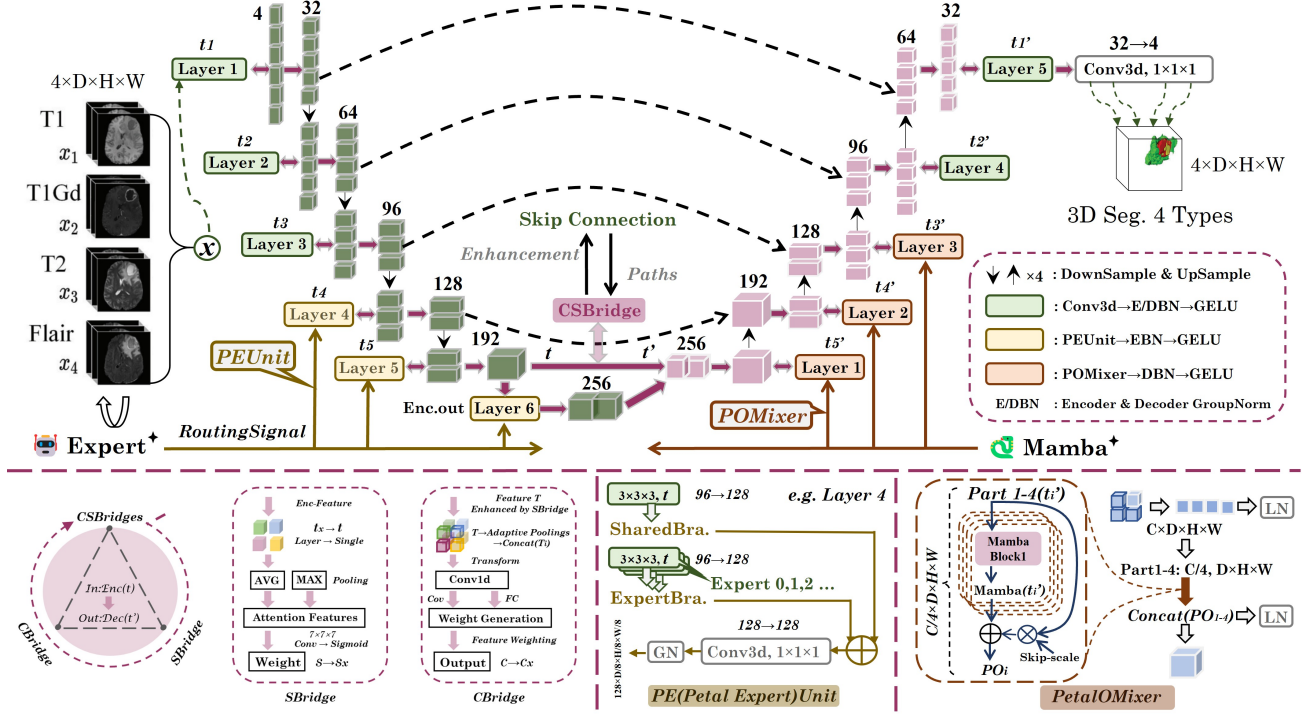


Figure 2. **Overall architecture of M⁴Fuse.** (a) CSBridge (CSB, feature fusion stage): CSB connects the encoder and decoder to enhance multi-scale features by integrating the spatial-channel attention of SBridge and CBridge: $\text{Dec}(t') = \text{Enc}(t) + t \cdot \text{SBridge}(t) + \text{CBridge}(t)$, where $t' = t \cdot s_x + c_x + t_x$ is fed to the decoder. Each decoder stage fuses with its corresponding subsampled encoder feature through residual skip connections. Here, skip connections provide propagation paths, while CSB acts as a feature enhancer to mitigate detail loss from encoder downsampling and insufficient reference cues during decoder upsampling. (b) Petal Expert Unit (PEU): Located at the encoder backend, PEU uses a shared-branch plus expert-branch design to handle multimodal and multidataset variation, enabling the encoder to capture both general anatomy and dataset-specific lesion patterns. (c) POMixer (POM): Placed at the decoder frontend, POM treats 3D features as sequences and uses Mamba to model long-range dependencies while jointly aggregating spatial and channel information, helping the decoder preserve local details and global semantics during high-resolution reconstruction.

3.3. Cross Scale Dual Stage Gating Bridge

Skip connections pass fine structure yet they also propagate modality-specific noise and scanner artifacts. We purify and align encoder features before decoding in two stages. The sigmoid is $\sigma(\cdot)$. Element-wise multiplication is \odot . The operator Conv_7 is a three-dimensional convolution with kernel size seven that maps two input channels to one attention map. The operators $\text{Avg}(t_s)$ and $\text{Max}(t_s)$ are channel-wise average and maximum giving tensors in $\mathbb{R}^{B \times 1 \times D_s \times H_s \times W_s}$. For each scale s a spatial attention mask is computed and applied

$$\begin{cases} a_s = \sigma(\text{Conv}_7([\text{Avg}(t_s), \text{Max}(t_s)])) \in \mathbb{R}^{B \times 1 \times D_s \times H_s \times W_s}, \\ t_s^{\text{SP}} = a_s \odot t_s \in \mathbb{R}^{B \times C_s \times D_s \times H_s \times W_s}. \end{cases} \quad (7)$$

Global average pooling over spatial axes is $\text{GAP}(\cdot)$. Per-scale channel statistics are $z_s = \text{GAP}(t_s^{\text{SP}}) \in \mathbb{R}^{B \times C_s}$. Concatenation over scales gives $z = [z_1 \parallel z_2 \parallel z_3 \parallel z_4 \parallel z_5] \in \mathbb{R}^{B \times C_\Sigma}$ where $C_\Sigma = \sum_s C_s$. For each scale a channel gate

uses weights $W_s \in \mathbb{R}^{C_\Sigma \times C_s}$ and bias $b_s \in \mathbb{R}^{C_s}$

$$g_s = \sigma(z W_s + b_s) \in \mathbb{R}^{B \times C_s}. \quad (8)$$

The vector g_s is broadcast along spatial axes to match t_s^{SP} . Two nonnegative learned scalars α and β control residual strength

$$\begin{cases} \hat{t}_s = t_s + \alpha t_s^{\text{SP}} + \beta (g_s \odot t_s^{\text{SP}}), \\ \alpha \geq 0, \quad \beta \geq 0. \end{cases} \quad (9)$$

Since $\sigma : \mathbb{R} \rightarrow (0, 1)$, we have $\|a_s\|_\infty \leq 1$ and $\|g_s\|_\infty \leq 1$. Using any submultiplicative norm, the bridge is bounded as

$$\|\hat{t}_s\| \leq (1 + \alpha + \beta) \|t_s\|. \quad (10)$$

The bridge is applied once to $\{t_1, t_2, t_3, t_4, t_5\}$ and the bridged tensors are reused in the decoder.

3.4. Shared Plus Expert Routing

Acquisition protocols differ across centers and cohorts. A single shared pathway is often suboptimal whereas a fully

Algorithm 1 M⁴Fuse Forward Pass

- 1: **Input** volume $x \in \mathbb{R}^{B \times C \times D \times H \times W}$: B mini-batch size, C modalities, D, H, W spatial sizes
 - 2: **Input** id vector $d \in \{1, \dots, M\}^B$: one expert index per sample
 - 3: **Input** operators: Conv3D (3D conv), GN (group norm), Pool (strided pooling), Up (trilinear up-sampling), POM (grouped state-space mixer), PEU (shared-plus-expert unit), CSB (cross-scale dual-stage bridge), Conv1 $\times 1 \times 1$ (pointwise 3D conv)
 - 4: $t_1 = \text{GN}(\text{Conv3D}(x))$
 - 5: $t_2 = \text{GN}(\text{Conv3D}(\text{Pool}(t_1)))$
 - 6: $t_3 = \text{GN}(\text{Conv3D}(\text{Pool}(t_2)))$
 - 7: $u_4 = \text{Pool}(t_3)$
 - 8: $t_4 = \text{GN}(\text{PEU}_4(u_4, d))$
 - 9: $u_5 = \text{Pool}(t_4)$
 - 10: $t_5 = \text{GN}(\text{PEU}_5(u_5, d))$
 - 11: $b = \text{PEU}_b(\text{Pool}(t_5), d)$
 - 12: $(\tilde{t}_1, \tilde{t}_2, \tilde{t}_3, \tilde{t}_4, \tilde{t}_5) = \text{CSB}(t_1, t_2, t_3, t_4, t_5)$
 - 13: $y_1 = \text{GN}(\text{POM}(b)) + \tilde{t}_5$
 - 14: $y_1 = \text{Up}(y_1)$
 - 15: $y_2 = \text{GN}(\text{POM}(y_1)) + \tilde{t}_4$
 - 16: $y_2 = \text{Up}(y_2)$
 - 17: $y_3 = \text{GN}(\text{POM}(y_2)) + \tilde{t}_3$
 - 18: $y_3 = \text{Up}(y_3)$
 - 19: $y_4 = \text{GN}(\text{Conv3D}(y_3)) + \tilde{t}_2$
 - 20: $y_4 = \text{Up}(y_4)$
 - 21: $y_5 = \text{GN}(\text{Conv3D}(y_4)) + \tilde{t}_1$
 - 22: **Output** logits $\hat{y} = \text{Conv1} \times 1 \times 1(y_5)$
-

specialized network is heavy. We adopt a compact shared-plus-expert unit at high semantic layers. The shared mixer is f_{sh} . The expert mixers are $\{f_m\}_{m=1}^M$. For sample i the high-level input is $u_i \in \{t_4, t_5, b\}$. A top-one expert index is $\pi(u_i) \in \{1, \dots, M\}$ which can be assigned by a dataset identifier. The unit output for sample i is

$$\text{PEU}(u_i) = f_{\text{sh}}(u_i) + f_{\pi(u_i)}(u_i). \quad (11)$$

A top- K variant averages the selected experts' outputs. To stabilize gradients, we use batch-wise concatenation instead of in-place assignment, with dropout $p \in [0, 1)$

$$\text{PEU}(u) = \text{Dropout}_p \left(f_{\text{sh}}(u) + \text{concat}_i \left(f_{\pi(u_i)}(u_i) \right) \right). \quad (12)$$

Here concat_i denotes concatenation along the batch dimension. Algorithm 1 summarizes the forward path and Algorithm 2 summarizes the bridge.

3.5. Network Variants

M⁴Fuse (Input Resolution: 128 \rightarrow 4) has three variants:

- *M⁴Fuse-T*: $\text{Max}(C) = 128, \text{SEL} = \{128, 4, 4, 4\}$

Algorithm 2 Cross-scale dual-stage gating bridge

- 1: **Input** features $(t_1, t_2, t_3, t_4, t_5)$ with shapes $t_s \in \mathbb{R}^{B \times C_s \times D_s \times H_s \times W_s}$
 - 2: **Input** weights $\{W_s\}$ with $W_s \in \mathbb{R}^{C_\Sigma \times C_s}$; biases $\{b_s\}$ with $b_s \in \mathbb{R}^{C_s}$; scalars α, β with $\alpha \geq 0, \beta \geq 0$
 - 3: **Input** operators: σ (sigmoid), \odot (element-wise product), Conv₇ (three-dimensional conv, kernel size seven), GAP (global average pooling), Avg (channel-wise average), Max (channel-wise maximum), concat (channel-wise concatenation)
 - 4: **for** $s \in \{1, 2, 3, 4, 5\}$ **do**
 - 5: $a_s = \sigma(\text{Conv}_7([\text{Avg}(t_s), \text{Max}(t_s)]))$
 - 6: $t_s^{\text{SP}} = a_s \odot t_s$
 - 7: **end for**
 - 8: $z = \text{concat}(\text{GAP}(t_1^{\text{SP}}), \dots, \text{GAP}(t_5^{\text{SP}}))$
 - 9: **for** $s \in \{1, 2, 3, 4, 5\}$ **do**
 - 10: $g_s = \sigma(zW_s + b_s)$; broadcast g_s to shape of t_s^{SP}
 - 11: $\hat{t}_s = t_s + \alpha t_s^{\text{SP}} + \beta (g_s \odot t_s^{\text{SP}})$
 - 12: **end for**
 - 13: **Output** $(\hat{t}_1, \hat{t}_2, \hat{t}_3, \hat{t}_4, \hat{t}_5)$
-

- *M⁴Fuse-S*: $\text{Max}(C) = 196, \text{SEL} = \{196, 4, 4, 4\}$
- *M⁴Fuse-B*: $\text{Max}(C) = 256, \text{SEL} = \{256, 4, 4, 4\}$
- *M⁴Fuse-L*: $\text{Max}(C) = 384, \text{SEL} = \{384, 4, 4, 4\}$

where C and SEL represent the maximum number of network channels and the Size of the Enc.out Layer (SEL), respectively.

4. Experiments

Datasets. The proposed M⁴Fuse model was trained and tested on two challenging multimodal brain tumor datasets (BraTS2019, BraTS2021), with each 3D brain MRI volume containing four modalities (T1, T1ce, T2, T2-FLAIR) and three segmentation targets (WT: Whole Tumor, ET: Enhancing Tumor, TC: Tumor Core). BraTS2019 (335 volumes, low/high-grade [LGG/HGG] gliomas) serves as the core reference for comparisons, quantifications, and ablation benchmarks. BraTS2021 adopts unified data grading to extend low-resolution scenarios, with its visual comparisons further validating the model's lightweight, efficiency, and generalization. Given inter-dataset grading discrepancies, different expert counts were configured during training/comparisons (Note: The expert mechanism adapts to lesion type, location, and modality variations across datasets; see **Supplementary Table S2.1**).

BraTS2019 used five-fold cross-validation (80% training, 20% validation per fold) to ensure result stability and reliability. BraTS2021 data was randomly split into training/validation/test sets at a 6:2:2 ratio, with the validation set excluded from gradient training.

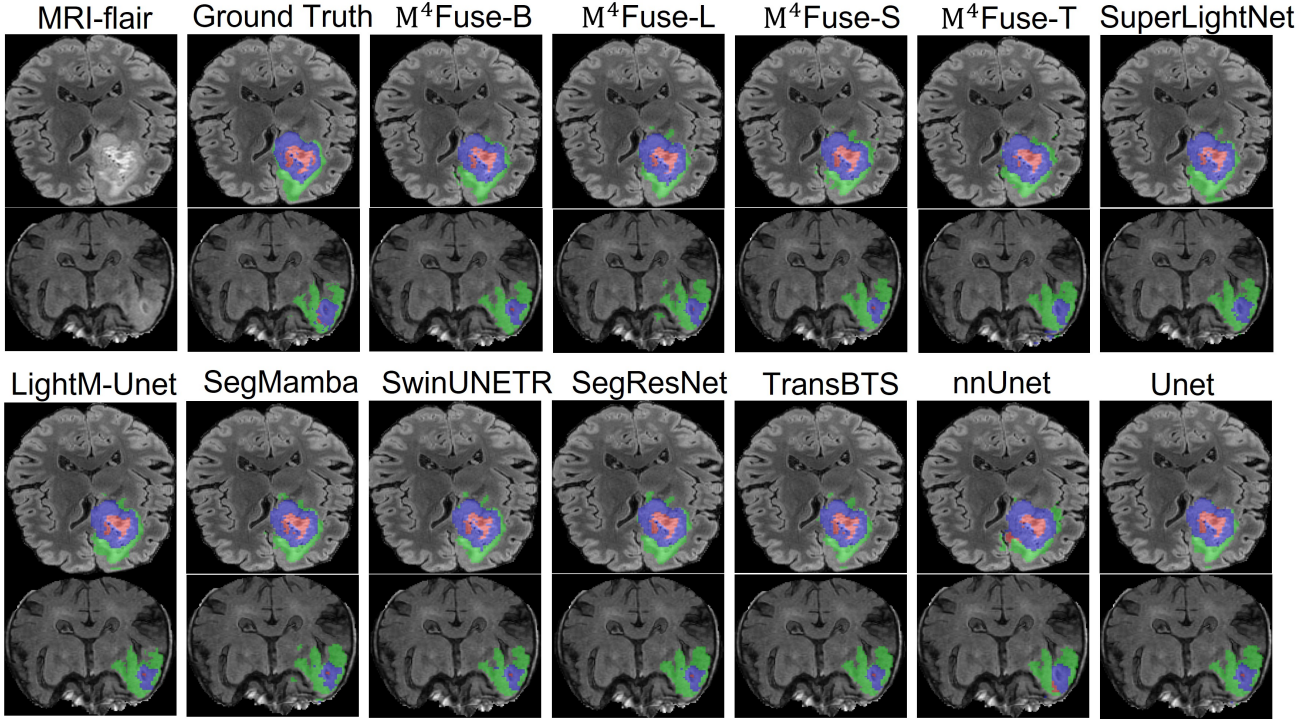


Figure 3. Visualized segmentation of BraTS 2021 datasets, input resolution: $64 \times 128 \times 128$, where red indicates tumor core, blue indicates whole tumor, and green indicates enhancing tumor.

Table 1. Performance comparison with SOTA methods on BraTS2019 validation set using 5-Cross-Validation Mode and BraTS2021 validation set using Train-Valid-Eval Mode. The mean performance (Dice %, HD95 mm and #params M) of all models combinations is shown here (due to space limit, the detailed each stage from different modes performance of 5-fold and TvE metrics is given in **supplementary Table S1**). Top-k=1/2 signifies the MoE module’s specialized extraction and sharing of training expertise across data types or modalities, while simultaneously enabling internal comparisons between datasets.

Methods	Params (M)	BraTS2021 (Top-k=1, IRS=1.04M)								BraTS2019 (Top-k=2, IRS=2.09M)								
		Dice \uparrow (%)				HD95 \downarrow (mm)				Dice \uparrow (%)				HD95 \downarrow (mm)				
		WT	TC	ET	Avg	WT	TC	ET	Avg	WT	TC	ET	Avg	WT	TC	ET	Avg	
3D Unet [6]	12.34	87.91	85.61	78.22	83.91	3.81	3.32	3.11	3.41	84.72	74.07	67.49	75.42	8.81	13.58	13.43	9.48	
nnUnet [12]	31.19	89.26	87.58	84.77	87.34	3.20	2.55	2.89	2.88	87.43	79.71	76.79	81.31	4.87	5.16	5.29	5.10	
TransBTS [29]	31.65	88.43	85.78	78.58	84.26	6.63	3.61	3.03	4.42	87.52	79.23	76.22	80.99	4.68	4.98	3.99	4.55	
SegResNet [19]	18.80	89.59	89.42	82.67	87.22	3.17	2.64	2.47	2.76	88.71	82.08	74.28	81.69	3.99	5.48	5.02	4.83	
SwinUNETR [11]	62.19	89.29	86.74	78.88	84.97	3.24	2.65	2.74	2.87	88.16	80.73	75.82	81.57	4.00	4.93	5.17	4.70	
SegMamba [31]	66.85	90.48	85.54	84.01	88.23	3.97	2.55	2.12	2.88	89.11	82.25	75.71	82.35	4.28	5.65	5.77	5.23	
LightM-Unet [15]	5.02	89.99	87.27	80.45	85.90	3.47	2.48	2.34	2.76	88.70	80.20	72.43	80.44	4.68	5.18	4.67	4.84	
SuperLightUnet [36]	2.97	90.57	89.23	86.33	88.70	3.40	2.53	2.11	2.68	88.54	80.64	74.32	81.16	4.74	6.36	5.33	5.47	
Top-k=1/2	M ⁴ Fuse-T	0.29/0.32	87.01	85.97	81.73	84.90	4.08	3.18	2.56	3.27	88.31	81.00	72.95	80.75	3.70	4.88	4.07	4.21
	M ⁴ Fuse-S	0.63/0.70	88.82	88.23	86.72	87.92	4.25	2.70	2.12	3.02	88.66	82.12	74.38	81.72	5.41	5.52	4.93	5.28
	M ⁴ Fuse-B	1.11/1.23	89.14	89.74	87.49	88.79	3.66	2.42	1.90	2.66	89.31	82.69	75.16	82.38	4.14	4.46	4.75	4.51
	M ⁴ Fuse-L	2.45/2.72	89.33	90.17	85.89	88.46	3.83	2.57	1.88	2.76	88.89	81.74	75.51	82.04	3.30	4.50	4.30	4.03

Implementation details. Our model was implemented in Python 3.8, PyTorch 2.0, and MONAI 1.3, with training and inference conducted on A100 GPUs. For the training and validation of M⁴Fuse’s, the BraTS 2019 and

BraTS 2021 datasets were randomly cropped to fixed sizes of $128 \times 128 \times 128$ (IRS=2.09M) and $64 \times 128 \times 128$ (IRS=1.04M) respectively, with a unified batch size of 2 adopted for both datasets. The AdamW optimizer was em-

ployed with an initial learning rate of $1e-4$, a weight decay of $1e-5$ and a minimum learning rate of $1e-6$, whose learning rate was dynamically adjusted by a cosine annealing scheduler during training. The loss function was constructed as a weighted combination of Dice Loss and Cross Entropy Loss with a weight ratio of 7:3. For dataset partitioning, 5-Fold Cross-Validation was used for BraTS 2019, and the BraTS 2021 dataset was randomly split into training, validation and test sets at a ratio of 6:2:2; early stopping with a patience of 80 (monitoring total Dice coefficient) was applied for the training of BraTS 2019 to avoid overfitting. The total training epochs were set to 200 for BraTS 2019 and 300 for BraTS 2021, with gradient scaling (AMP) and TF32 acceleration techniques utilized to optimize training efficiency. In the inference phase, Test Time Augmentation was adopted to enhance the robustness of the model’s prediction results.

4.1. Comparison with others

Table 1 shows experimental results on BraTS2019 and BraTS2021. M^4 Fuse achieves excellent segmentation performance and parameter efficiency, with Dice scores of 82.38% and 88.79%, surpassing SegMamba (82.35%) and SuperLightUnet (88.70%) by 0.03% and 0.09%, respectively. With 62.63% fewer parameters than SuperLightUnet, it significantly outperforms other models. Additionally, this model achieves the best HD95 metric on the BraTS2019 dataset.

Figure 3 shows qualitative segmentation comparisons on BraTS2021 (Flair modality as background, two samples). M^4 Fuse converges more stably and rapidly during training. The upper panel reveals lower ET region tissue segmentation loss and more precise segmentation and the lower panel demonstrates superior WT/ET region consistency, boundary handling, and reduced oversegmentation.

To address the core parameter count issue, we quantified and compared structural parameter distributions across models from Table 2. Notably, only 3D Unet, nnUnet, SwinUNETR, and our model show balanced parameter allocations across modules, validating architectural robustness. Most lightweight models rely on plug-and-play modules (e.g., Mobile backbones for encoders, FLD [18] for decoders), merely assembling components to achieve the final overall module quantification—failing to achieve fundamental lightweighting. In contrast, our method embeds diverse mechanisms in UNet, such as data-adaptive specialized modules and the CSBridge attention enhancer (integrated with skip connections to maximize encoder feature utilization for segmentation). Finally, our Base model shows consistent segmentation metric decline with reduced input resolution. For Training/Inference Memory and GFLOPS comparisons, see **Supplementary Table S3**.

Table 2. Quantitative evaluations with 4×128^3 (IRS=2.09M).

Methods	Parameter Structure (M)			In Res Params	
	#encoder	#decoder	else (CSB/.)		
3D Unet	6.12 (49.59%)	6.22 (50.41%)	-	128^3	12.34
nnUnet	5.09 (16.33%)	3.07 (9.85%)	23.02 (73.81%)	128^3	31.19
TransBTS	31.58 (99.81%)	0.07 (0.19%)	-	128^3	31.65
SegResNet	17.59 (93.56%)	1.12 (6.44%)	-	128^3	18.80
SwinUNETR	13.70 (22.03%)	16.94 (27.24%)	1.54 (50.73%)	128^3	62.19
SegMamba	60.87 (91.06%)	5.97 (8.94%)	-	128^3	66.85
LightM-Unet	4.94 (98.53%)	0.08 (1.47%)	-	128^3	5.02
SuperLightUnet	2.70 (91.07%)	0.26 (8.88%)	-	128^3	2.97
M^4 Fuse-T (0.5 \times)	0.12 (43.3%)	0.09 (33.6%)	0.06 (23.0%)	128^3	0.32
M^4 Fuse-S (0.75 \times)	0.27 (42.9%)	0.21 (33.6%)	0.14 (23.5%)	128^3	0.70
M^4 Fuse-B	0.59 (47.9%)	0.37 (30.0%)	0.26 (21.1%)	128^3	1.23
M^4 Fuse-L (1.5 \times)	1.03 (42.4%)	0.82 (33.5%)	0.59 (24.1%)	128^3	2.72
M^4 Fuse-B (2 \times V.)	(Dice: 82.30 HD95: 5.23)			64×128^2	1.23

4.2. Ablation Study

We analyze the architecture factors that determine lightweight accuracy in multimodal 3D brain tumor segmentation, the overall trend in Table 3 is that capacity must be placed where it preserves discriminative cues rather than widened uniformly, moving from a plain CNN baseline to adding sample level domain experts raises Dice from 75.42% to 80.12% and reduces HD95 from 9.48 to 5.87 at a modest parameter increase, inserting a Mamba style mixer without first cleaning and aligning the skips lowers Dice to 75.46% because long range modeling amplifies cross site noise when skip pathways are unstandardized, adding the cross scale dual stage bridge restores and surpasses performance to 82.38% Dice and 4.51 HD95 at about 1.23M parameters and the PetaloMixer ratio reaches 100.0%, the data support a know why account in which global processing is effective only after spatial denoising and cross scale channel realignment, the decoder then benefits from clean evidence and the model no longer needs a wide high semantic path to approximate missing context, this explains why a half volume input of $64 \times 128 \times 128$ remains sufficient under our design and why the base configuration is Pareto efficient on accuracy versus parameters.

The controlled studies in Table 4 and Table 6 explain the mechanism and isolate causes, Top-1 expert routing with Softmax gating gives the best Dice at 81.09% while Top-2 and ADS gates reduce Dice to 75.54% and 75.59% because simultaneous expert activation introduces interference which is unnecessary when domain cues are sample specific, fusion at pixel or token level preserves boundary sharpness and yields 81.02% to 81.14% Dice whereas channel only aggregation drops to 77.50% because it over smooths modality dependent edges, early or late single point fusion underperforms while middle multi layer fusion improves both Dice and HD95 because it aligns semantics before upsampling, within the bridge the spatial and channel stages are complementary and their combina-

Table 3. M⁴Fuse overall ablation (Dice coefficient %, 95th percentile Hausdorff distance in voxels).

#	Methods	PMRatio	Params	Dice↑	HD95↓
0	E2E- ¹ Fuse → CNN (*Unet)	0.08%	*0.01	75.42	9.48
1	¹ Fuse+PEU- ² Fuse → CNN+MoE	48.7%	0.60	-	-
2	¹ Fuse+ ² Fuse+POM- ³ Fuse → CNN+MoE+Mamba	78.8%	0.97	75.46	6.10
3	¹Fuse+²Fuse+³Fuse+CSB-⁴Fuse → Cycle-LiqBE (CNN+MoE+Mamba) ↑	100.0%	1.23	82.38	4.51

Table 4. Ablation of fusion configurations for the Shared-Plus-Expert Unit and the Cross-Scale Dual-Stage Gating Bridge (Dice coefficient %, 95th percentile Hausdorff distance in voxels).

*PEUnit-Training-Fusion Config. #CSBridge-Fusion Config.	Fusion Mode	Dice↑	HD95↓
*Softmax + Top-1	Gate	81.09	4.97
*Softmax + Top-2	Gate	75.54	6.54
*Gumbel-softmax (ADS)	Gate	75.59	6.47
*Mini-attention→Exp.W	Gate	77.78	5.05
*Learned Bias + Gate	Gate	75.49	6.22
*Patch Level (Splicing)	Granularity	80.85	4.68
*Token Level (MHSA-Fusion)	Granularity	81.14	4.20
*Channel Level (SE)	Granularity	77.50	5.82
*Pixel (Ours) + Channel	Granularity	81.02	4.66
#Shallow → Deep (t3, t4)	Scale	77.81	6.40
#Deep → Shallow (t5, E.o)	Scale	77.66	5.34
#Jump (t5', t4', t3')	Scale	78.29	5.77
#Random (CSB) /batch	Scale	-	-
#Group (t4-CB, t5-SB, E.o-CSB)	Scale	-	-
#Early stage (t1 → once)	Period	78.16	5.22
#Middle stage (t3, t4)	Period	-	-
#Late stage (t5')	Period	77.99	5.43
#Bottleneck stage (E.o)	Period	-	-
#Funnel stage (t1-t3-CB, t4-E.o-CSB)	Period	-	-

Table 5. Controlled decoder-width sweep on BraTS2019 (3 seeds, mean±std).

Setting	α	Params(M) ↓	GFLOPs ↓	Dice(%) ↑	HD95(mm) ↓
Raw skip (w/o CSB)	0.5	0.76	70.78	80.32±5.08	4.89±1.87
Raw skip (w/o CSB)	1.0	1.03	193.93	83.07±3.96	4.88±1.96
Raw skip (w/o CSB)	2.0	2.00	681.76	84.28±4.49	5.36±2.12
Purified skip (with CSB)	0.5	1.02	72.42	81.95±4.28	10.64±3.95
Purified skip (with CSB)	1.0	1.29	195.57	84.83±3.32	5.99±2.62
Purified skip (with CSB)	2.0	2.26	683.41	81.66±4.70	5.32±1.71

Table 6. Ablation of core modules: Cross-Scale Dual-Stage Gating Bridge, Shared-Plus-Expert Unit, and PetaloMixer (Dice coefficient %, 95th percentile Hausdorff distance in voxels).

*CSB Config. *PEU Config. #POM Config.	SB Route	CB Share	CSB Expert LinProj.	Dice↑	HD95↓
*CSB1 (Re-CSB)	×	×	×	75.46	6.10
*CSB2	✓	×	×	76.15	6.21
*CSB3	×	✓	×	78.38	5.81
&PEU1 (Re-MoE)	×	×	×	-	-
&PEU2	✓	×	✓	75.51	6.50
&PEU3	✓	✓	×	77.53	5.14
&PEU4 (Top-1)	✓	✓	✓	-	-
#POM1	✓	✓	×	75.84	6.50
#POM2	✓	×	✓	76.60	5.11
#POM3 (!parts)	×	✓	✓	75.63	6.44
#POM4	×	×	✓	76.00	6.18
#POM5	✓	×	×	76.86	5.04

tion is consistently superior, within the mixer the grouped scan, the residual skip scale, and a single linear projection each contribute and removing any part degrades Dice or inflates HD95, taken together the evidence shows that encoder and decoder capacity should be balanced and guided by denoised and aligned skips and that global modeling should remain linear time and placed after purification, this yields strong accuracy at 1.23M parameters and explains why heavy symmetric decoders or attention first designs are compute heavy and brittle on BraTS style heterogeneity.

Table 5 provides a controlled intervention. Two trends emerge. (i) Raw skip: widening the decoder remains beneficial. (ii) Purified skip: after skip purification, widening shows diminishing/negative returns. This is exactly the intended evidence for our decoder marginal utility claim, and it also explains why the larger variant (decoder-wider) does not outperform the base model.

5. Conclusion

M⁴Fuse addresses brittleness and inefficiency in volumetric tumor segmentation caused by encoder–decoder imbalance and reliance on large input volumes. Rather than uniformly widening the network, it allocates capacity to the most informative stages via a grouped state space mixer for linear-time long-range modeling, a cross-scale dual-stage gating bridge for skip-feature denoising and alignment, and sample-level domain experts at high-semantic, low-resolution layers for center- and protocol-robust adaptation with linearly controllable parameters. Extensive analyses and ablations reveal a decoder marginal utility principle: once skip features are purified and aligned, enlarging the decoder or high-semantic pathway yields limited gains and may degrade contrast-sensitive microstructures such as ET, whereas targeted capacity allocation and selective gating remain effective. The base model achieves strong accuracy with only 1.11M parameters, matching or surpassing heavier and lightweight state-of-the-art models with lower memory and FLOPs, placing it on a favorable accuracy–efficiency Pareto frontier. Results suggest that clinical 3D segmentation should favor clean skip connections and selective global context over wider decoders and larger inputs. Future work will extend this design to add automatic routing cues, and clarify how state-space parameters influence fine-structure sensitivity.

Acknowledgments

This work was supported by the Scientific Research Project of Higher Education Institutions in Anhui Province (No. 2024AH053451) and the Anhui Province 2025 University Science and Engineering Teachers Enterprise Secondment Practice Program (No. 2025jsqygz42).

References

- [1] Yasmina Al Khalil, Sina Amirrajab, Cristian Lorenz, Jürgen Weese, Josien Pluim, and Marcel Breeuwer. Reducing segmentation failures in cardiac mri via late feature fusion and gan-based augmentation. *Computers in Biology and Medicine*, 161:106973, 2023. 2
- [2] Dianlong An, Panpan Liu, Yan Feng, Pengju Ding, Weifeng Zhou, and Bin Yu. Dynamic weighted knowledge distillation for brain tumor segmentation. *Pattern Recognition*, 155: 110731, 2024. 1
- [3] Jeffrey G Andrews, Sarabjot Singh, Qiaoyang Ye, Xingqin Lin, and Harpreet S Dhillon. An overview of load balancing in hetnets: Old myths and open problems. *IEEE Wireless Communications*, 21(2):18–25, 2014. 2
- [4] Guogang Cao, Zhaojun Yang, Wanying Liang, Sai Zhang, Tao Zhong, Hongdong Mao, Dong Wang, and Ming Zong. Lcmf-net: A lightweight collaborative multimodal fusion network for brain tumor segmentation. *Neural Networks*, page 108257, 2025. 3
- [5] Shiyi Cao, Shu Liu, Tyler Griggs, Peter Schafhalter, Xiaoxuan Liu, Ying Sheng, Joseph E Gonzalez, Matei Zaharia, and Ion Stoica. Moe-lightning: High-throughput moe inference on memory-constrained gpus. In *Proceedings of the 30th ACM International Conference on Architectural Support for Programming Languages and Operating Systems, Volume 1*, pages 715–730, 2025. 2
- [6] Özgün Çiçek, Ahmed Abdulkadir, Soeren S. Lienkamp, Thomas Brox, and Olaf Ronneberger. 3d u-net: Learning dense volumetric segmentation from sparse annotation. In *Medical Image Computing and Computer-Assisted Intervention – MICCAI 2016*, pages 424–432, Cham, 2016. Springer International Publishing. 2, 6
- [7] Rizhi Ding, Hui Lu, and Manhua Liu. Denseformer-moe: A dense transformer foundation model with mixture of experts for multi-task brain image analysis. *IEEE Transactions on Medical Imaging*, 2025. 2
- [8] Yongkang Ding, Xiaoyin Wang, Hao Yuan, Meina Qu, and Xiangzhou Jian. Decoupling feature-driven and multimodal fusion attention for clothing-changing person re-identification. *Artificial Intelligence Review*, 58(8):241, 2025. 2
- [9] Bowen Dong, Yilong Fan, Yutao Sun, Zhenyu Li, Tengyu Pan, Zhou Xun, and Jianyong Wang. Maximum score routing for mixture-of-experts. In *Findings of the Association for Computational Linguistics: ACL 2025*, pages 12619–12632, 2025. 2
- [10] Shaofeng He, Qiu Cheng, Yu Huai, Zhongke Zhu, and Jie Ding. Mixture-of-experts for semantic segmentation of remote sensing image. In *International Conference on Image Processing and Artificial Intelligence (ICIPAI 2024)*, pages 478–483. SPIE, 2024. 2
- [11] Yufan He, Vishwesh Nath, Dong Yang, Yucheng Tang, Andriy Myronenko, and Daguang Xu. Swinunetr-v2: Stronger swin transformers with stagewise convolutions for 3d medical image segmentation. In *Medical Image Computing and Computer Assisted Intervention – MICCAI 2023*, pages 416–426, Cham, 2023. Springer Nature Switzerland. 2, 6
- [12] Fabian Isensee, Paul F Jaeger, Simon AA Kohl, Jens Petersen, and Klaus H Maier-Hein. nnu-net: a self-configuring method for deep learning-based biomedical image segmentation. *Nature methods*, 18(2):203–211, 2021. 3, 6
- [13] Huafeng Li, Zengyi Yang, Yafei Zhang, Wei Jia, Zhengtao Yu, and Yu Liu. Mulfs-cap: Multimodal fusion-supervised cross-modality alignment perception for unregistered infrared-visible image fusion. *IEEE Transactions on Pattern Analysis and Machine Intelligence*, 2025. 2
- [14] Yunlong Liang, Fandong Meng, and Jie Zhou. THOR-MoE: Hierarchical task-guided and context-responsive routing for neural machine translation. In *Proceedings of the 63rd Annual Meeting of the Association for Computational Linguistics (Volume 1: Long Papers)*, pages 21433–21445, Vienna, Austria, 2025. Association for Computational Linguistics. 2
- [15] Weibin Liao, Yinghao Zhu, Xinyuan Wang, Chengwei Pan, Yasha Wang, and Liantao Ma. Lightm-unet: Mamba assists in lightweight unet for medical image segmentation. *arXiv preprint arXiv:2403.05246*, 2024. 2, 6
- [16] Huabing Liu, Zhengze Ni, Dong Nie, Dinggang Shen, Jinda Wang, and Zhenyu Tang. Multimodal brain tumor segmentation boosted by monomodal normal brain images. *IEEE Transactions on Image Processing*, 33:1199–1210, 2024. 1
- [17] Xiao Liu, Peng Gao, Tao Yu, Fei Wang, and Ru-Yue Yuan. Cswin-unet: Transformer unet with cross-shaped windows for medical image segmentation. *Information Fusion*, 113: 102634, 2025. 1
- [18] Yi Liu, Lutao Chu, Guowei Chen, Zewu Wu, Zeyu Chen, Baohua Lai, and Yuying Hao. Paddleseg: A high-efficient development toolkit for image segmentation, 2021. 2, 7
- [19] Andriy Myronenko. 3d mri brain tumor segmentation using autoencoder regularization. In *Brainlesion: Glioma, Multiple Sclerosis, Stroke and Traumatic Brain Injuries*, Cham, 2019. Springer International Publishing. 6
- [20] Dichao Pan, Jianguo Shen, Zaid Al-Huda, and Mohammed AA Al-Qaness. Vcanet: Vision transformer with fusion channel and spatial attention module for 3d brain tumor segmentation. *Computers in Biology and Medicine*, 186: 109662, 2025. 1
- [21] Soujanya Poria, Erik Cambria, Rajiv Bajpai, and Amir Husain. A review of affective computing: From unimodal analysis to multimodal fusion. *Information fusion*, 37:98–125, 2017. 2
- [22] Abhiram Potlapalli and Seetharam Khetavath. Exploring the use of deep learning models for image compression in embedded systems: Encoder and decoder architectures. *Journal of Intelligent Systems & Internet of Things*, 15(1), 2025. 1
- [23] Novsheena Rasool and Javaid Iqbal Bhat. A critical review on segmentation of glioma brain tumor and prediction of

- overall survival. *Archives of Computational Methods in Engineering*, 32(3):1525–1569, 2025. 1
- [24] Olaf Ronneberger, Philipp Fischer, and Thomas Brox. U-net: Convolutional networks for biomedical image segmentation. In *International Conference on Medical image computing and computer-assisted intervention*, pages 234–241. Springer, 2015. 1, 2
- [25] Abhishek Srivastava, Debesh Jha, Sukalpa Chanda, Umada Pal, Håvard D. Johansen, Dag Johansen, Michael A. Riegler, Sharib Ali, and Pål Halvorsen. Msrf-net: A multi-scale residual fusion network for biomedical image segmentation. *IEEE Journal of Biomedical and Health Informatics*, 26(5):2252–2263, 2022. 2
- [26] Dayu Tan, Zhiyuan Yao, Xin Peng, Haiping Ma, Yike Dai, Yansen Su, and Weimin Zhong. Multi-level medical image segmentation network based on multi-scale and context information fusion strategy. *IEEE Transactions on Emerging Topics in Computational Intelligence*, 8(1):474–487, 2023. 2
- [27] Haonan Wang, Peng Cao, Jinzhu Yang, and Osmar Zaiane. Narrowing the semantic gaps in u-net with learnable skip connections: The case of medical image segmentation. *Neural Networks*, 178:106546, 2024. 1
- [28] Huiyan Wang, Ruihao Peng, Ming Ying, Fashuai Li, Jiuyi Zhang, Xiaolan Li, Yan Tian, and Guofeng Zhang. Mff-sdd: A bidirectional guidance and multiscale multimodal fusion model for small defect detection in industrial films. *IEEE Transactions on Industrial Informatics*, 2025. 2
- [29] Wenxuan Wang, Chen Chen, Meng Ding, Hong Yu, Sen Zha, and Jiangyun Li. Transbts: Multimodal brain tumor segmentation using transformer. In *Medical Image Computing and Computer Assisted Intervention – MICCAI 2021*, pages 109–119, Cham, 2021. Springer International Publishing. 2, 6
- [30] Yikai Wang, Wenbing Huang, Fuchun Sun, Tingyang Xu, Yu Rong, and Junzhou Huang. Deep multimodal fusion by channel exchanging. *Advances in neural information processing systems*, 33:4835–4845, 2020. 2
- [31] Zhaohu Xing, Tian Ye, Yijun Yang, Guang Liu, and Lei Zhu. Segmamba: Long-range sequential modeling mamba for 3d medical image segmentation. In *Medical Image Computing and Computer Assisted Intervention – MICCAI 2024*, pages 578–588, Cham, 2024. Springer Nature Switzerland. 2, 6
- [32] Guoan Xu, Juncheng Li, Guangwei Gao, Huimin Lu, Jian Yang, and Dong Yue. Lightweight real-time semantic segmentation network with efficient transformer and cnn. *IEEE Transactions on Intelligent Transportation Systems*, 24(12):15897–15906, 2023. 2
- [33] Zihui Xue and Radu Marculescu. Dynamic multimodal fusion. In *Proceedings of the IEEE/CVF Conference on Computer Vision and Pattern Recognition*, pages 2575–2584, 2023. 2
- [34] Yuanhang Yang, Shiyi Qi, Wenchao Gu, Chaozheng Wang, Cuiyun Gao, and Zenglin Xu. XMoE: Sparse models with fine-grained and adaptive expert selection. In *Findings of the Association for Computational Linguistics: ACL 2024*, pages 11664–11674, Bangkok, Thailand, 2024. Association for Computational Linguistics. 2
- [35] Zhiwen Yang, Haowei Chen, Ziniu Qian, Yang Yi, Hui Zhang, Dan Zhao, Bingzheng Wei, and Yan Xu. All-in-one medical image restoration via task-adaptive routing. In *International Conference on Medical Image Computing and Computer-Assisted Intervention*, pages 67–77. Springer, 2024. 2
- [36] Feng Yu, Jiacheng Cao, Li Liu, and Minghua Jiang. Superlightnet: Lightweight parameter aggregation network for multimodal brain tumor segmentation. In *Proceedings of the Computer Vision and Pattern Recognition Conference*, pages 5197–5206, 2025. 2, 6
- [37] Hong Zhang, Junxue Zhang, Wei Bai, Kai Chen, and Mosharaf Chowdhury. Resilient datacenter load balancing in the wild. In *Proceedings of the Conference of the ACM Special Interest Group on Data Communication*, pages 253–266, 2017. 2
- [38] Xian Zhang, Zhibin Quan, Qiang Li, Dejun Zhu, and Wankou Yang. Sed: Searching enhanced decoder with switchable skip connection for semantic segmentation. *Pattern Recognition*, 149:110196, 2024. 1
- [39] Zheng Zhang, Yaqi Xia, Hulin Wang, Donglin Yang, Chuang Hu, Xiaobo Zhou, and Dazhao Cheng. Mpmoe: Memory efficient moe for pre-trained models with adaptive pipeline parallelism. *IEEE Transactions on Parallel and Distributed Systems*, 35(6):998–1011, 2024. 2
- [40] Meihua Zhou, Jun Feng, Tianlong Zheng, Min Cheng, and Li Yang. Contrast-aware hybrid attention network for medical image segmentation. *Information Sciences*, page 123000, 2025. 2
- [41] Meihua Zhou, Xinyu Tong, Jiarui Zhao, Min Cheng, Li Yang, Lei Tian, and Nan Wan. Dcl-se: Dynamic curriculum learning for spatiotemporal encoding of brain imaging. *arXiv preprint arXiv:2511.15151*, 2025. 2
- [42] Meihua Zhou, Tianlong Zheng, Zhihua Wu, Nan Wan, and Min Cheng. Damnet: Dynamic mobile architectures for alzheimer’s disease. *Computers in Biology and Medicine*, 185:109517, 2025. 2
- [43] Sihang Zhou, Dong Nie, Ehsan Adeli, Jianping Yin, Jun Lian, and Dinggang Shen. High-resolution encoder–decoder networks for low-contrast medical image segmentation. *IEEE Transactions on Image Processing*, 29:461–475, 2019. 1
- [44] Tongxue Zhou. M2gcnet: Multi-modal graph convolution network for precise brain tumor segmentation across multiple mri sequences. *IEEE Transactions on Image Processing*, 2024. 1
- [45] Rongxin Zhu, Azzedine Boukerche, and Qiuling Yang. An efficient secure and adaptive routing protocol based on gmm-hmm- lstm for internet of underwater things. *IEEE Internet of Things Journal*, 11(9):16491–16504, 2024. 2
- [46] Zhiqin Zhu, Ziyu Wang, Guanqiu Qi, Neal Mazur, Pan Yang, and Yu Liu. Brain tumor segmentation in mri with multi-modality spatial information enhancement and boundary shape correction. *Pattern Recognition*, 153:110553, 2024. 1